

## Dynamics of Fracture in Drying Suspensions

E. R. Dufresne,<sup>\*,†,‡</sup> D. J. Stark,<sup>†,‡</sup> N. A. Greenblatt,<sup>†</sup> J. X. Cheng,<sup>§,||</sup> J. W. Hutchinson,<sup>†</sup>  
L. Mahadevan,<sup>†</sup> and D. A. Weitz<sup>†,‡</sup>

DEAS, Department of Physics, and Department of Chemistry and Chemical Biology, Harvard University,  
Cambridge, Massachusetts 02138

Received May 4, 2006. In Final Form: June 22, 2006

We investigate the dynamics of fracture in drying films of colloidal silica. Water loss quenches the nanoparticle dispersions to form a liquid-saturated elastic network of particles that relieves drying-induced strain by cracking. These cracks display intriguing intermittent motion originating from the deformation of arrested crack tips and aging of the elastic network. The dynamics of a single crack exhibits a universal evolution, described by a balance of the driving elastic power with the sum of interfacial power and the viscous dissipation rate of flowing interstitial fluid.

Drying has been exploited for thousands of years in protective coatings and ceramics. In fact, this process is so familiar that “watching paint dry” has become synonymous with tedium. However, drying presents a number of outstanding scientific and technological problems. Drying drives suspensions far from equilibrium: for typical samples of macroscopic dimensions at ambient conditions, fluid can leave faster than particles can relax into their equilibrium configurations. Consequently, the macroscopic material properties of drying suspensions can be heterogeneous in both space and time. Recent experiments and theory have described the steady consolidation of suspended particles into close-packed networks driven by the flow of fluid to a pinned liquid–vapor interface.<sup>1–4</sup> The formation of homogeneous solids by this process is often frustrated by mechanical instabilities, such as fracture and buckling, resulting in diverse and beautiful morphology<sup>5–13</sup> but limiting the utility of the films.<sup>14,15</sup> The growth of cracks in drying films tracks the consolidation of particles that proceeds continuously; surprisingly, however, individual cracks exhibit a pronounced intermittent motion. This ubiquitous feature of fracture dynamics remains mysterious and suggests that essential elements may be missing from our understanding of the drying process.

\* Corresponding author. Current address: Departments of Mechanical Engineering, Chemical Engineering, and Physics, Yale University, New Haven, Connecticut. E-mail: eric.dufresne@yale.edu.

† DEAS, Harvard University.

‡ Department of Physics, Harvard University.

§ Department of Chemistry and Chemical Biology, Harvard University.

|| Current address: Weldon School of Biomedical Engineering, Purdue University, West Lafayette, Indiana 47907.

(1) Deegan, R. D.; Bakajin, O.; Dupont, T. F.; Huber, G.; Nagel, S. R.; Witten, T. A. *Nature* **1997**, *389*, 828.

(2) Routh, A. F.; Russel, W. B. *Ind. Eng. Chem. Res.* **2001**, *40*, 4302.

(3) Dufresne, E. R.; Corwin, E. I.; Greenblatt, N. A.; Ashmore, J.; Wang, D. Y.; Dinsmore, A. D.; Cheng, J. X.; Xie, X. S.; Hutchinson, J. W.; Weitz, D. A. *Phys. Rev. Lett.* **2003**, *91*, 224501.

(4) Tirumkudulu, M. S.; Russel, W. B. *Langmuir* **2004**, *20*, 2947.

(5) Allain, C.; Limat, L. *Phys. Rev. Lett.* **1995**, *74*, 2981.

(6) Komatsu, T.; Sasa, S. *Jpn. J. Appl. Phys., Part 1* **1997**, *36*, 391.

(7) Hull, D.; Caddock, B. D. *J. Mater. Sci.* **1999**, *34*, 5707.

(8) Shorlin, K. A.; deBruyn, J. R.; Graham, M.; Morris, S. W. *Phys. Rev. E* **2000**, *61*, 6950.

(9) Lee, W. P.; Routh, A. F. *Langmuir* **2004**, *20*, 2947.

(10) Neda, Z.; Leung, K. t.; Jozsa, L.; Ravasz, M. *Phys. Rev. Lett.* **2002**, *88*, 095502.

(11) Pauchard, L.; Adda-Bedia, M.; Allain, C.; Couder, Y. *Phys. Rev. E* **2003**, *67*, 027103.

(12) Goehring, L.; Morris, S. W. *Europhys. Lett.* **2005**, *69*, 739.

(13) Tsapis, N.; Dufresne, E. R.; Sinha, S. S.; Riera, C. S.; Hutchinson, J. W.; Mahadevan, L.; Weitz, D. A. *Phys. Rev. Lett.* **2005**, *94*, 018302.

(14) Brinker, C.; Scherer, G. W. *Sol–Gel Science: The Physics and Chemistry of Sol–Gel Processing*; Academic Press: New York, 1990.

(15) Egen, M.; Zentel, R. *Chem. Mater.* **2002**, *14*, 2176.

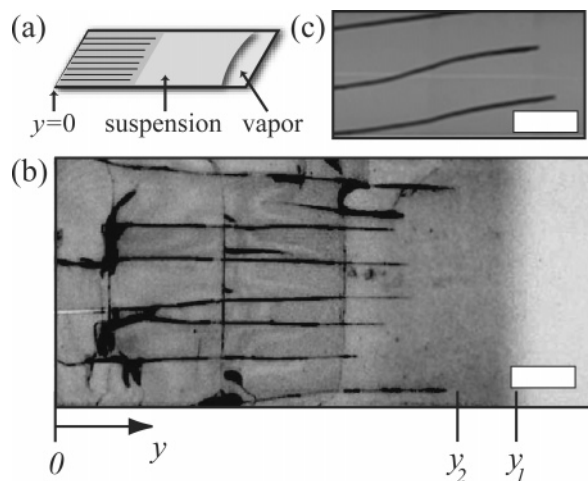


**Figure 1.** Fracture in a drying suspension. (a) Schematic diagram of the drying geometry. (b) Epifluorescent micrograph of a drying film (inverted contrast).  $y_1$  is the compaction front, and  $y_2$  is the crack front. (c) CARS micrograph tuned to the O–H stretch at  $3500\text{ cm}^{-1}$ . The brightness is proportional to the local water concentration. Scale bars are  $500\text{ }\mu\text{m}$ .

In this letter, we describe measurements of the dynamics of fracture in drying nanoparticle suspensions over seven decades in time. Over long time intervals, individual cracks advance in discrete jumps because of differences between the stresses required to initiate and continue fracture. At shorter time intervals, the speed of individual jumps is limited by the viscous flow of fluid within the deforming particle network.

We study the unidirectional drying of confined thin films. We exploit capillary forces to load aqueous suspensions of monodisperse colloidal silica nanoparticles with radii of  $a = 11\text{ nm}$  (Ludox AS-40) into glass tubes (Vitrocom) with a  $100 \times 2000\text{ }\mu\text{m}^2$  rectangular cross section, as shown schematically in Figure 1a. The rate of evaporation from the filling end,  $y = 0$ , is much greater than that from the opposite end, which lies several millimeters from the edge of the open glass tube.

As fluid evaporates, a macroscopic flow consolidates particles behind the drying surface, as shown in Figure 1b. To visualize this process, we add a small quantity of fluorescent carboxylate-modified polystyrene nanoparticles (IDC), radius  $10\text{ nm}$ , at a volume fraction of  $10^{-3}$ . Between the filling end and the compaction front,  $y = y_1$ , particles are close-packed with a spatially averaged volume fraction of  $\phi_C = 0.58 \pm 0.08$ .<sup>3</sup> This close-packed region fractures with intriguing arrays of cracks, roughly

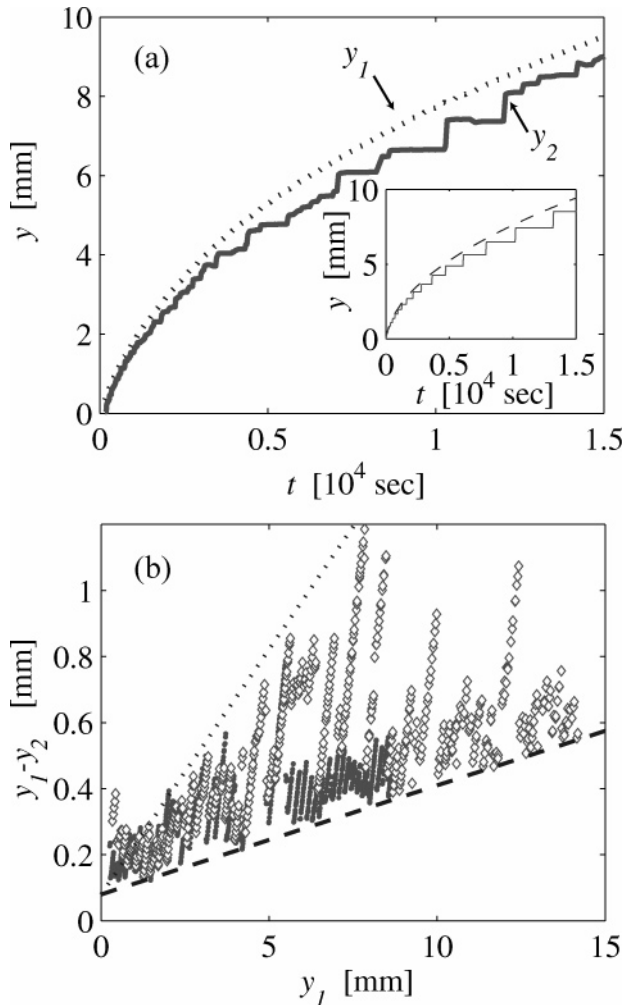


**Figure 2.** Crack dynamics at long time intervals. (a) Trajectories of the compaction front,  $y_1$ , (dotted line) and crack front,  $y_2$ , (thick solid line). (Inset) Simulated compaction and crack front trajectories. (b) Separation of the compaction front and crack front,  $y_1 - y_2$ , vs the location of the compaction front,  $y_1$ . Open and closed symbols are for two experiments with identical setups. The slopes of the dotted and dashed lines give  $\sigma_{go}/\sigma(0)$  and  $\sigma_{stop}/\sigma(0)$ , respectively.

aligned with the  $y$  axis. At the compaction front, the particle volume fraction drops rapidly to its initial value,  $\phi_i = 0.2$ . We analyze digital images to locate the positions of the compaction front and individual crack tips. The position of the leading crack tip,  $y_2$ , is designated as the crack front.

The compaction front advances smoothly as the suspension dries. The measured trajectory,  $y_1(t)$ , is plotted as a dotted line in Figure 2a. Particles are deposited in the close-packed region as fluid flows from the bulk of the sample to replenish water lost at the surface to evaporation.<sup>1</sup> This macroscopic flow is driven by capillary forces. A similar mechanism is responsible for the flow of fluid through a tree.<sup>16</sup> As water evaporates from the drying surface, nanometer-scale menisci form in the gaps between particles. The pressure in the water just inside the air/water interface is  $2\gamma/r_M$  below atmospheric pressure, where  $\gamma$  is the surface tension and  $r_M$  is the local radius of curvature of the interface. The pressure increases from the edge of the sample to the compaction front, which remains near atmospheric pressure. This pressure gradient drives flow to the drying edge as described by Darcy's law,  $J = -(k/\eta)\nabla P$  where  $J$  is the fluid flux,  $k$  is the

permeability of the porous close-packed region,  $\eta$  is the viscosity of the interstitial fluid, and the pressure gradient is  $\nabla P \approx 2\gamma/r_M y_1$ . For randomly packed monodisperse spheres,  $k$  can be estimated using the Carmen–Kozeny equation<sup>14</sup>

$$k = \frac{1}{45} \frac{(1 - \phi_C)^3}{\phi_C^2} a^2$$

In the early stages of drying, fluid flows to the surface at a steady rate to replenish fluid lost by evaporation. As the compact region grows, its hydrodynamic resistance increases, and the menisci increase their curvature, maintaining fluid flow to keep up with evaporation. Eventually, the curvature reaches a geometric limit set by the pore size,  $r_P \approx 0.15a$ . At this point, the advance of the compaction front becomes limited by the rate of fluid flow to the surface and begins to slow.<sup>17</sup> In both regimes, the compaction front trajectory is well described by

$$\frac{y_1(t)}{y_0} = \sqrt{1 + \frac{2t}{t_0}} - 1 \quad (1)$$

where  $y_0$  and  $3t_0/2$  are the length and time where the dynamics crosses over from being evaporation- to flow-limited.<sup>3</sup>

Capillary forces not only drive the growth of the compact region but also drive its fracture. The distribution of water in a drying film is visualized by a coherent anti-Stokes Raman scattering (CARS) micrograph of a drying film, shown in Figure 1c. Whereas the material surrounding the cracks is wet, the cracks are free of liquid water on the inside. Because gas diffuses freely through the empty cracks, they remain at atmospheric pressure. However, the fluid surrounding the cracks has a large negative pressure. This pressure difference is equivalent to a tensile stress,  $\sigma$ , which drives the cracks forward. The absolute values of the tensile stress can be quite high. Throughout the flow-limited regime of the growth of the compact region, the stress at the drying surface remains constant at  $\sigma(0) = 2\gamma/r_P$ . For our 11-nm-radius spheres, this corresponds to  $\sigma(0) = 80 \text{ MPa} = 800 \text{ atm}$ .

Whereas the advance of the compaction front is steady, the crack front,  $y_2(t)$ , moves intermittently, as shown in Figure 2a. Even though these stochastic trajectories vary from experiment to experiment, they share many features. First, all trajectories have a characteristic “staircase” shape. Second, the crack front lags behind the compaction front, and the distance between them,  $y_1 - y_2$ , is constrained by minimum and maximum values that increase as the two advance. This is illustrated in Figure 2b, where we plot  $y_1 - y_2$  against  $y_1$  for two separate experiments. If we assume that the close-packed region is homogeneous, then the tension in the fluid decreases linearly from the drying edge to the compaction front,  $\sigma(y)/\sigma(0) = 1 - y/y_1$ . Thus, the lines constraining the trajectories in Figure 2b represent lines of constant tension. The dashed line constraining the minimum values of  $y_1 - y_2$  can be interpreted as the stress at which a running crack tip must arrest,  $\sigma_{stop} = 2.8 \text{ MPa}$ . Similarly, the dotted line limiting the maximum values of  $y_1 - y_2$  corresponds to the stress at which an arrested crack must begin to run,  $\sigma_{go} = 12.6 \text{ MPa}$ .

The characteristic steplike trajectory of the crack front is a direct consequence of the fact that  $\sigma_{go} > \sigma_{stop}$ . As the compaction front advances, the stress throughout the film increases monotonically over time. An arrested crack tip remains stationary

(17) Evaporation is slowed by a minute recession of the air/water interface into the bulk of the sample. Because the pore size is much smaller than the mean free path of water vapor, the transport of vapor through the pore space is in the Knudsen limit where the diffusion coefficient is significantly reduced. Thus, even the slowest evaporation rates observed in this experiment can be obtained with a recession of the air/water interface of less than  $100 \mu\text{m}$ .

(16) Taiz, L.; Zeiger, E. *Plant Physiology*; Sinauer Associates: Sunderland, MA, 2002.

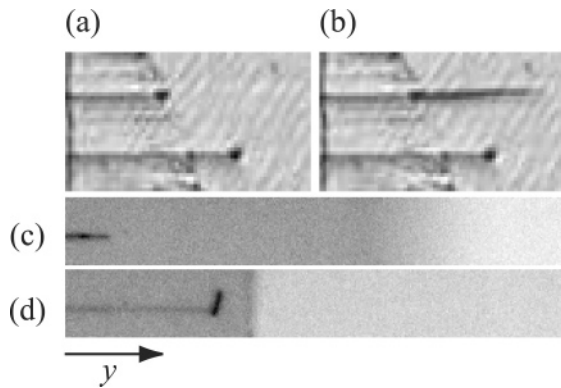


**Figure 3.** Deformation of arrested crack tips. Bright-field micrographs of a drying suspension (a) just before and (b) during a crack jump, demonstrating changes in the crack tip morphology. Field of view:  $420 \times 240 \mu\text{m}^2$ . Stress-induced destabilization. Epifluorescent micrograph (inverted contrast) of a drying suspension (a) just before evaporation is interrupted and (b) 7000 s later. Field of view:  $750 \times 10 \mu\text{m}^2$ .

until the local stress exceeds  $\sigma_{\text{go}}$ , when it rapidly jumps toward the compaction front, stopping at  $\sigma(y) = \sigma_{\text{stop}}$ . Combining this dynamical rule with a linear stress profile and eq 1 for compaction front motion, we simulate crack and compaction front trajectories and plot the results in Figure 2a (inset). The results capture salient features of crack dynamics over times from 10 to  $10^4$  s, including intermittent motion and increasing jump length. However, this deterministic model does not yield the stochastic component of crack front trajectories that must arise from interactions between cracks or from inhomogeneities in the film.

For a single crack, the stress required to advance depends on material properties and geometrical factors. In a thin elastic film, the elastic energy released as a crack moves forward an infinitesimal length  $dL$  is  $\alpha\sigma^2h^2 dL/E$ , where  $h$  is the thickness of the film and  $E$  is the elastic modulus. The  $\alpha$  parameter depends on the relative elastic moduli and the adhesion of the film and the substrate. We assume that the film has a much lower modulus than the substrate. Thus,  $\alpha = 0.5$  if the film is bound on both sides, and  $\alpha = 1.25$  if it is bound on one side only.<sup>18</sup> In the quasistatic limit, all bulk elastic energy is converted to surface energy of the crack,  $\Gamma h dL$ , where  $\Gamma$  is the energy of the crack surface per unit area. Therefore, a crack can propagate as long as tensile stress exceeds  $\sigma_c = \sqrt{(E\Gamma)/(\alpha h)}$ .

Our system, however, is not characterized by a single critical stress,  $\sigma_c$ , but by two distinct stresses  $\sigma_{\text{go}} \neq \sigma_{\text{stop}}$ . There are two possible causes for this difference: changes either in crack tip geometry or in material properties of the film. First, arrested crack tips are observed to blunt and/or split within seconds of arrest, reducing the concentration of stress at the tip that is essential for continued motion, as demonstrated in Figure 3a and b. Second, the material properties of the particle network vary in both space and time. Even though no change in the volume fraction is visible near the crack tips, differences in the mechanical properties of the compact region are dramatically demonstrated by the relaxation of the drying film when evaporation is arrested. We seal both ends of the capillary tube with vacuum grease and image the evolution of the film over long time intervals. Just before evaporation is stopped, the compaction front is diffuse, as shown in Figure 3c. Afterward, particles in the first few hundred micrometers of the close-packed region diffuse away slowly, leaving behind a sharp interface of close-packed particles *in equilibrium* with a lower volume fraction fluid suspension, as

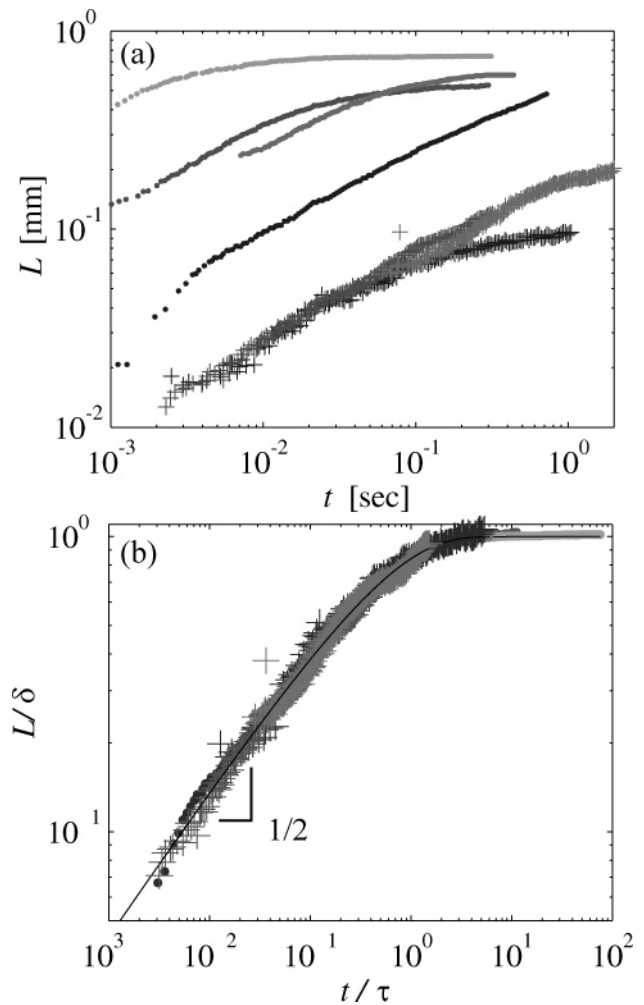


**Figure 4.** Crack dynamics at short time intervals. (a) Seven individual crack jumps from a few different samples. (b) Scaled trajectories, symbols, and master curve (line).

shown in Figure 3d. Thus, adhesive forces between particles in the film vary significantly in space and time. These differences are due to the irreversible destabilization of the close-packed particles to form a robust elastic network at a critical value of the fluid tension. Similar time-dependent material properties play a governing role in the onset of buckling of drying colloidal droplets<sup>13</sup> and have been suggested to contribute to the mechanical properties of green ceramic films.<sup>19</sup>

Our simple two-stress model captures the intermittent dynamics of crack tips over long time intervals but assumes that cracks jump to their final positions instantaneously. To go beyond this unrealistic assumption, we acquire bright-field images of single cracks using a high-speed camera (Phantom v5.0) and capture the fast dynamics of cracks over short times, from  $10^{-3}$  to 1 s. The trajectories of several individual crack jumps,  $L(t)$ , are shown in Figure 4a. Although there is tremendous variability in the magnitudes of jump lengths and speeds, all cracks evolve similarly; they advance like  $\sqrt{t}$  at early times before slowing and stopping at their final positions.

A simple energy balance can describe the shape of these individual crack trajectories. In contrast to a conventional molecular solid, the opening of a single crack in a fluid-saturated particle network drives the flow of interstitial fluid. Therefore, at finite rates of propagation, energy must be consumed by viscous flow. When  $\sigma > \sigma_c$ , the amount of elastic energy released from the bulk

(18) Hutchinson, J. W.; Suo, Z. *Adv. Appl. Mech.* **1992**, *29*, 63.

(19) Chiu, R. C.; Cima, M. J. *J. Am. Ceram. Soc.* **1993**, *76*, 2769.

exceeds the energy consumed to create new surface area and drives the flow of interstitial fluid. The rate of viscous dissipation in the porous particle network is given by  $\int (\eta J^2/k) dV$  where the flux of fluid from the tip is approximately  $J = (1 - \phi)\sin \theta \dot{L}$  and we have assumed a crack with a triangular tip and a constant opening half-angle,  $\theta$ . This flow persists over a volume surrounding the crack roughly equal to the new volume of the crack (i.e.,  $\int dV \approx whL$ ). Combining these approximations, we estimate the rate of viscous dissipation to be  $(whL/\beta)\dot{L}^2$ , with  $\beta = k/(\eta(1 - \phi)^2\sin^2 \theta)$ . Equating the elastic power to the sum of the interfacial and viscous power yields an equation for the length of a single crack propagating through a fluid-saturated porous elastic material

$$\frac{dL}{dt} = \left[ 1 - \left( \frac{\sigma_c}{\sigma} \right)^2 \right] \frac{\beta \sigma}{2L} \quad (2)$$

where we have removed the explicit dependence on the crack width using  $w = 2\alpha h\sigma/E$ , which is valid for isolated cracks in a thin elastic film. In the early stages of a jump, the crack tip has travelled a short distance and the stress,  $\sigma$ , is relatively constant so that  $L(t) \approx \sqrt{t}$ . In this regime, steady deceleration of the crack is due to the rapidly increasing viscous dissipation around the tip. However, as the crack advances, it moves into regions of lower stress and finally arrests where  $\sigma = \sigma_c$ . Assuming a linear stress profile along the direction of propagation, eq 2 simplifies to

$$\frac{d\tilde{L}}{d\tilde{t}} = \frac{1}{2} \left( \frac{1}{\tilde{L}} - 1 \right) \quad (3)$$

Here we have nondimensionalized length using the length of the jump,  $\delta$ , and time using  $\tau = \delta^2/\beta\sigma_0$ , where  $\sigma_0$  is the stress at the beginning of the jump. The parameter  $\beta\sigma_0$  varies widely, from 0.06 to 260 mm<sup>2</sup>/s. Near the end of a jump, the crack tip trajectory is exponential,  $\tilde{L} \approx 1 - \exp(-\tilde{t}/2)$ . The solution of eq 3 can be expressed in closed form over the full range of  $\tilde{L}$  using the Lambert

$W$  function,  $W[x]$ :<sup>20</sup>

$$\tilde{L}(\tilde{t}) = 1 + W \left[ -\exp \left( -1 - \frac{\tilde{t}}{2} \right) \right] \quad (4)$$

All crack trajectories are well fit by this form, as is clearly demonstrated by scaling the trajectories by the fitted values of  $\tau$  and  $\delta$  plotted in Figure 4b. The scaled trajectories collapse onto a single master curve, given by eq 4, plotted as a thin solid line. A more detailed model, accounting for interactions between cracks and incorporating a rigorous formulation of the coupling between elastic deformation and viscous flow<sup>21</sup> is needed to predict the scaling parameters accurately.

These results highlight the complex interplay of interfacial forces, fluid flow, and heterogeneous mechanical properties inherent to the mechanics of drying suspensions. An improved understanding of the mechanics of drying suspensions will lead to advancements in materials processing using drying films while forming an accessible model system for investigating broader issues in dynamic poroelastic fracture, with potential impact in larger-scale geophysical phenomena.

**Acknowledgment.** We thank J. Ashmore, M. Brenner, J. Rice, H. Stone, and fellow members of the Cracking Club (R. Buscall, S. Morris, A. Routh, W. Russel, M. Tirumkudulu, and L. White) for enlightening discussions. We acknowledge X. S. Xie for access to his CARS microscope and NSF through the Harvard MRSEC (DMR-0213805) for support.

LA061251+

(20) Corless, R. M.; Gonnet, G. H.; Hare, D. E. G.; Jeffrey, D. J.; Knuth, D. E. *Adv. Comput. Math.* **1996**, *5*, 329.

(21) Wang, H. F. *Theory of Linear Poroelasticity with Applications to Geomechanics and Hydrogeology*; Princeton University Press: Princeton, NJ, 2000.